

Piezoelectric Response in WO₃-x Thin Films by Aluminum Clustering

Pamela Pineda-Domínguez

Universidad Autónoma de Ciudad Juárez

Manuel Ramos (✉ manuel.ramos@uacj.mx)

Universidad Autónoma de Ciudad Juárez

John Nogan

Center for Integrated Nanotechnologies

Oscar Alberto López-Galán

Universidad Autónoma de Ciudad Juárez

José Luis Enríquez-Carrejo

Universidad Autónoma de Ciudad Juárez

Torben Boll

Karlsruhe Institute of Technology

Abel Hurtado-Macías

Centro de Investigación en Materiales Avanzados

Jorge López-Gallardo

The University of Texas at El Paso

Yahir Garay

The University of Texas at El Paso

Héctor Camacho-Montes

Universidad Autónoma de Ciudad Juárez

Martin Heilmaier

Karlsruhe Institute of Technology

Research Article

Keywords: tungsten trioxide, aluminum, piezoelectric, atom probe tomography, materials.

Posted Date: April 7th, 2021

DOI: <https://doi.org/10.21203/rs.3.rs-384370/v1>

License:   This work is licensed under a Creative Commons Attribution 4.0 International License.

[Read Full License](#)

Loading [MathJax]/jax/output/CommonHTML/jax.js

Abstract

We report piezoelectric response of $d_{33} = 35 \pm 5 \text{ pm V}^{-1}$ on aluminum doped tungsten trioxide thin films (Al-WO_{3-x}), prepared by RF-sputtering and post annealing treatment in air atmosphere. Using XPS characterization indicate a stoichiometry of $\text{WO}_{2.7}$ and Raman a distorted octahedral tungsten vibration mode of monoclinic WO_3 at 236.9 cm^{-1} , 691 cm^{-1} and 803 cm^{-1} corresponding to O-W-O chemical bonds. The grazing incidence X-ray diffraction revealed a non-centrosymmetric monoclinic ($P2_1/c$) and tetragonal ($P4/nmm$) mixed phases of WO_{3-x} with islands of piezoelectric domains as observed by atomic force microscope, additionally atom probe tomography revealed diffusion of aluminum ions from Al_2O_3 substrate.

1.0 Introduction

Outstanding applications in the field of Internet of Things (IoT) [1]–[3] and micro-electromechanical systems (MEMS) [4, 5] have increased the demand for environmentally friendly, low cost, and reliable materials to fabricate several types of sensors, actuators and power components [6–9]. This has expanded the interest on properties such as electrochromism and piezoelectricity in various materials [10–12]. Piezoelectric materials have gained importance in modern day technology due their wide range of applications, from positioners in electronic microscopes, crystal oscillators, sound and vibration sensors, and energy harvesting devices [13–19]. Piezoelectricity occurs mainly in non-centrosymmetric structures [20]–[23], which refers to those lacking an inversion point, i.e., a point or atom position at specific coordinates inside the Bravais unit cell, with respect to a crystallographic plane; in the spatial distribution this causes uneven distribution of electronic states and when a mechanical force is applied part of those accumulated electron charges are released, causing a piezoelectric response, as described extensively in the literature [21], [24]–[28]. Several materials can exhibit piezoelectricity to some degree, this includes ceramic materials [20], [29], polymers [23, 24] and semiconductors [31], with lead zirconate titanate, also known as PZT, is one of most common piezoelectric ceramics as reported in the literature, with remarkable piezoelectric response derived from interaction at morphotropic phase boundary (MPB) [25]. Sustainable environmental concerns and also that it is an insulator [27, 28] has caused an intensified on-going research worldwide in search for lead-free conducting piezoelectric materials [27, 29, 30], and previous investigations in the materials field indicate that piezoelectric semiconductors are potential candidates due to intrinsic piezoelectricity and conductivity [36]. Also, some binary compounds such as ZnO and AlN, have been considered attractive piezoelectric materials and currently are under extensive research [25, 32], some reports indicates addition of ZnO or WO_3 as dopants in PZT or in BaTiO_3 – SrTiO_3 ceramics can induce piezo-response [33–36]. Recently, Chen *et al.* successfully used ZnO- WO_{3-x} nanorods for piezoelectric-photoelectrochemical water splitting due to intrinsic ZnO piezoelectricity and the fact that WO_{3-x} charge carrier concentration can be tuned in function of oxygen vacancies [42]. Corby *et al.* found that vacancy concentration of 2% for stoichiometric oxides meaning oxygen concentration, can maximize photocurrent in water splitting performance [43], similar to the

Loading [MathJax]/jax/output/CommonHTML/jax.js

results reported by Soltani *et al.* [44]. Kim *et al.* reported piezoelectric response in an oxygen-deficient $WO_{2.96}$ film with a d_{33} coefficient of 7.9 pm/V, attributed to the non-centrosymmetric structures within film thickness, that corresponds to monoclinic and tetragonal phases [45]. In this communication, we are reporting piezoelectric response for aluminum doped WO_3 thin films annealed at 400°C, along with extensive characterization by grazing incidence X-ray diffraction (GIXRD) and atom probe tomography (APT).

2.0 Results And Discussion

Piezoelectric response by PFM

WO_3 thin films were deposited on sapphire with a resulting thickness of 225 nm and subsequently annealed at various temperatures, see experimental methods section. A piezoelectric response was found in the film annealed at 400°C, determined by characterization using piezo force microscopy technique in dual AC resonance tracking (DART) mode, as described extensively in [22, 26–28, 46, 47]. The surface topography of this film is shown in Fig. 1a, and Fig. 1b) and 1c) corresponds to the piezo force microscopy signal phase before and after measurements, revealing a local hysteresis loops; hysteresis loops corresponding to red circles, where piezo response domains appear as yellow, white and violet colored regions show polarization direction piezoelectric domains, as described by Kholkin *et al.* [27]. The white regions are positive domains, i.e., polarization pointing towards the bottom electrode, which occurred by switching domains as observed in hysteresis loops shown in Fig. 1e. Furthermore, ferroelectric behavior was observed in the sample annealed at 400°C from hysteresis loops in phase and piezoelectric coefficient (d_{33}) versus AC applied bias voltage as shown in Fig. 1f. The piezoelectric coefficient was determined by positioning the cantilever across a large grain of $Al-WO_{3-x}$ (red circle). The amplitude (nm) versus AC bias voltage (V) exhibited a butterfly loop as presented in Fig. 1d and it is related to piezoelectric deformation under an applied AC bias voltage demonstrating a local polarization switching behavior [28]. The latter indicates that a phase difference of 180° polarization switching under DC bias voltage related to the existence of piezoelectric domains and local d_{33} coefficient can be estimated by $(V-V_1)d_{33} = D-D_1$, where D is the measured piezoelectric deformation or amplitude, V is applied voltage, D_1 is the piezoelectric deformation, and V_1 is the applied voltage at the intersection as described by Roelofs *et al.* [28]. The coercive voltage (2.7 V) was evaluated using the equation $(V_c^+ - V_c^-)/2$ where V_c^+ and V_c^- are the forward and reverse coercive bias voltages, respectively. The piezoelectric coefficient (d_{33}) of $35 \pm 5 \text{ pmV}^{-1}$ was measured at the maximum voltage of 10 V for the film annealed at 400°C, which is four times higher than that reported by Kim *et al.* [45] for $WO_{2.9}$ and the highest value found in the literature for this material, indicating a potential use in piezoelectric devices [48].

The measured d_{33} coefficient is assume to occur due to non-centrosymmetric phases in combination with potential oxygen vacancies and aluminum doping induced a different stoichiometric composition of WO_{3-x} films, mainly for those processed at 400°C in agreement with reports as found in the literature [38, 48–

57]. And confirmed by XPS measurements (Supplemental material) which reveals a stoichiometry of $WO_{2.7}$ in the surface of the film annealed at 400°C and in agreement with grazing incidence x-ray diffraction (GIXRD) and atom probe tomography (APT) as presented in this communication.

Crystallographic structure as determined by GIXRD

As presented in Fig. 2, an evolution of crystallinity occurred on the films from room temperature to annealing process at 400°C and 550 °C corresponding to polycrystalline amorphous structure, reflections at 23.1° corresponds to (001), (021) and (121) and corresponds to monoclinic WO_{3-x} phase (γ - WO_{3-x}) [57], [59]–[61] with space group $P2_1/c$, a tetragonal WO_{3-x} phase (α - WO_{3-x}) with $P4/nm$ space group is formed for sample at 400°C in agreement with literature [61, 62]. The Raman spectra indicate a distorted octahedral tungsten vibration mode of monoclinic WO_{3-x} at 236.9 cm^{-1} , 691 cm^{-1} and 803 cm^{-1} attributed to bending O-W-O bonds and symmetric/antisymmetric stretching of W-O bonds (see supplemental material). However, as the annealing temperature increased and evolution of phases occurred with γ - WO_{3-x} or α - WO_{3-x} for 500°C and 550°C, respectively as observed. Furthermore, diffractions at $\sim 37^\circ$ which corresponds to (111) planes of metallic aluminum (FCC), only appear at 400°C and not at 500°C and 550°C, our believe is that aluminum clusters is formed by interdiffusion from sapphire substrates (Al_2O_3) during annealing process, in agreement with Li *et al.* oxygen vacancies can promote defects and dislocation; and potentially can induce diffusion of aluminum ions on lattice sites within WO_3 [64]; because critical temperature of aluminum diffusion is reached at above 300°C in agreement with previous reports, and revealed by atom probe tomography, Fig. 3. Thus, segregated aluminum induces formation of mixed α - WO_{3-x} and γ - WO_{3-x} phases in agreement with previous reports [52], [65]; as it is described usually heavy metallic ions like induces recrystallization in thin films [66]. Also, metallic species such as gold (Au) induces phase change from triclinic to monoclinic in WO_3 [67]. In here, we were able to determine that aluminum is diffused creating changes on the electronic states mainly on island form over film and mixed monoclinic and tetragonal (α - WO_{3-x} and γ - WO_{3-x}) specially when is processed at 400°C, in agreement with Ahart *et al.* [25] and Ibrahim *et al.* [68] who explained in detail that mixed phases can produce a morphotropic phase boundary (MPB).

Chemical distribution by atom probe tomography

In order to investigate chemical volume distribution a series of atom probe tomography characterizations were completed, which is an abrasive technique used to obtain time of flight mass spectrometry from events occurred due to laser pulse ionic evaporation at high-vacuum as described in the literature [69], for all APT measurements a well-defined interface between WO_3 film and Al_2O_3 substrate was revealed. From mass spectrum it was possible to achieve chemical composition distribution mainly at the WO_3 film thickness (0-400nm) and traces of aluminum, oxygen and tungsten was found as shown in Fig. 3. Tungsten concentration remains around 27% during annealing process and oxygen concentration is about 70% at 400 °C with strong traces of aluminum ($\sim 3\%$) which forms clusters, as shown in Fig. 3a; it is our believe this clusters are formed during annealing process by ionic diffusion from sapphire

substrate due to voids occurred by oxygen vacancies which allowed aluminum ions to undergo onto WO_3 [56], [65], which is in agreement with mixed phases as encountered by grazing incidence x-ray diffraction. For sample processed at 500°C lower concentration ($> 1\%$) of aluminum ions is found and corresponds mainly to $\alpha\text{-WO}_{3-x}$ as shown in Fig. 3b and no traces of grain boundaries was found for all samples.

3.0 Conclusions

We report a piezoelectric response with $d_{33} = 35 \pm 5$ p/V for Al-WO_{3-x} in thin films processed at 400°C . The grazing incidence x-ray and atom probe indicates that piezo-response effect is caused by aluminum diffusion creating mixed phase between $\gamma\text{-WO}_{3-x}$ (monoclinic) and $\alpha\text{-WO}_{3-x}$ (tetragonal) corresponding to a non-centrosymmetric. And we found that at elevated annealing temperatures ($> 400^\circ\text{C}$) film recrystallizes in $\alpha\text{-WO}_{3-x}$ followed by $\gamma\text{-WO}_{3-x}$ causing a reorder to piezoelectric domains, as confirmed by atom probe tomography where no clustering of aluminum was encountered for sample processed at 500°C .

Experimental Methods

RF magnetron sputtering

The tungsten trioxide (WO_3) thin films were deposited by radio frequency magnetron sputtering technique using a 99.99% pure WO_3 disk as target and Al_2O_3 as substrate. The base pressure was set up to 1×10^{-6} Torr before allowing Ar into the chamber as plasma source. The deposition rate was 1 \AA/s , at a working pressure of 3 mTorr and 225 W of RF power. The wafer was cut into several samples for subsequent annealing process at temperatures of 300°C , 400°C , 500°C and 550°C , for 45 min with a 15 min ramp down, in air. A film thickness of ~ 220 nm was measured for the as-deposited film using profilometry.

Piezo Force Microscopy (PFM)

Domain imaging, switching and piezoelectric hysteresis loops were investigated by piezoresponse force microscopy (PFM) using the Dual AC Resonance Tracking (DART) mode, in a commercial Atomic Force Microscope (AFM) model Infinity 3D Asylum Research with two internal lock-ins amplifiers. The PFM was operated in vertical mode with an AC voltage amplitude of $5 V_{\text{pk-pk}}$ and at a drive frequency of 398 kHz far below the resonance of the cantilever, applied between the bottom electrode and the *Pt/Ir* conductive tip during imaging PFM. To achieve the measurement of local polarization (hysteresis loops) a voltage of -10 to $10 V_{\text{pk-pk}}$ was applied using the spectroscopy PFM mode.

Grazing Incidence X-Ray Diffraction (XRD)

Crystallographic structure was obtained with the aid of Panalytical Empyrean system, with $\text{Cu}_{K\alpha}$ radiation Loading [MathJax]/jax/output/CommonHTML/jax.js ng voltage of 40 kV and an emission current of 30 mA.

Scanning angle was varied from 20° to 80° with a step size of 0.05°.

Atom Probe Tomography (APT)

Three-dimensional chemical distribution for W, O and Al was obtained with a Cameca® LEAP 4000X high-resolution system, equipped with a UV laser ($\lambda \sim 355$ nm). All measurements were taken at a set temperature of 50 K with an evaporation rate of 0.2 and a laser frequency of 100 kHz. The laser beam was set to 20 pJ/V, and all data were reconstructed from SEM images using the Cameca IVAS® 3.6.14 package. Additional samples were prepared by directly coating the micro tip coupons provided by the CAMECA with the multilayer sputtering system. The samples were prepared by annular milling with the aid of the focused ion-beam (FIB) instrument models FEI® Strata or Zeiss Auriga, both equipped with dual beam. The surface was protected with an additional platinum layer deposited from a precursor gas within the SEM-FIBs to reduce amorphization of film matrix.

Declarations

Authors Contribution

P.M.P.D, M.R., J.N. and O.A.L.G. completed all sample preparation at Center for Integrated Nanotechnologies-Albuquerque, NM. J.L.E.C. and P.M.P.D. performed the Raman measurements. T.B. and M.H. performed atom probe tomography characterization at Karlsruhe Nano and Micro Facility. A. H.M. measure piezo-electric properties at Centro de Investigación en Materiales Avanzados-Chihuahua. J. L. and Y. G. performed XPS measurements at University of Texas at El Paso. Data analysis was completed by P.M.P.D., H.C. and O.A.L. G.; and manuscript was mainly typed by P.M. P.D., O. A. L.G., J.L.E.C., M.H. and M.R.

Acknowledgments

Authors thank: Center for Integrated Nanotechnologies, an Office of Science User Facility operated for the U.S. Department of Energy (DOE) Office of Science. Sandia National Laboratories is a multi-program laboratory managed and operated by Sandia Corporation, a wholly owned subsidiary of Lockheed Martin Corporation, for the U.S. Department of Energy's National Nuclear Security Administration under contract DE-AC04-94AL85000 under external user proposal #2018AU0133. We are grateful to the Karlsruhe Micro and Nano Facility (KNMF) of Karlsruhe Institute of Technology for usage of Atom Probe Tomography and FIB instruments and to IAM-WK of Karlsruhe Institute of Technology. The Laboratorio Nacional de Nanotecnología of Centro de Investigación en Materiales Avanzados (CIMAV-Chihuahua) for the usage of electron microscopy and characterization equipment. P. Pineda-Domínguez and M. Ramos thank Dirección General de Vinculación e Intercambio of Universidad Autónoma de Ciudad Juárez for travel award support and Instituto de Ingeniería y Tecnología of UACJ. Pineda-Domínguez thank the graduate scholarship sponsor program of Consejo Nacional de Ciencia y Tecnología-México, scholarship number

References

1. Cánovas, R., Parrilla, M., Blondeau, P. & Andrade, F. J. A novel wireless paper-based potentiometric platform for monitoring glucose in blood. *Lab Chip*. **17**, 142500–142507 <https://doi.org/10.1039/C7LC00339K> (2017).
2. Novell, M., Guinovart, T., Blondeau, P., Rius, F. X. & Andrade, F. J. A paper-based potentiometric cell for decentralized monitoring of Li levels in whole blood. *Lab Chip*. **14** (no. 7), 1308 <https://doi.org/10.1039/c3lc51098k> (2014).
3. Zanella, A., Bui, N., Castellani, A., Vangelista, L. & Zorzi, M. “Internet of Things for Smart Cities,” IEEE Internet Things J., vol. 1, no. 1, pp. 22–32, Feb 2014, doi: 10.1109/JIOT.2014.2306328.
4. Yuan, K. *et al.* “Fabrication of a Micro-Electromechanical System-Based Acetone Gas Sensor Using CeO₂ Nanodot-Decorated WO₃ Nanowires,” *ACS Appl. Mater. Interfaces*, vol. 12, no. 12, pp. 14095–14104, Mar. 2020, doi: 10.1021/acami.9b18863.
5. Andreu-Perez, J., Leff, D. R., Ip, H. M. D. & Yang, G. Z. “From Wearable Sensors to Smart Implants—Toward Pervasive and Personalized Healthcare,” *IEEE Trans. Biomed. Eng.*, vol. 62, no. 12, pp. 2750–2762, Dec 2015, doi: 10.1109/TBME.2015.2422751.
6. Kumar, A. Methods and Materials for Smart Manufacturing: Additive Manufacturing, Internet of Things, Flexible Sensors and Soft Robotics. *Manufacturing Letters*. **15**, 122–125 <https://doi.org/10.1016/j.mfglet.2017.12.014> (Jan. 2018).
7. Spearing, S. M. Materials issues in microelectromechanical systems (MEMS). *Acta Mater.* **48** (no. 1), 179–196 [https://doi.org/10.1016/S1359-6454\(99\)00294-3](https://doi.org/10.1016/S1359-6454(99)00294-3) (Jan. 2000).
8. Zaia, E. W., Gordon, M. P., Yuan, P. & Urban, J. J. Progress and Perspective: Soft Thermoelectric Materials for Wearable and Internet-of-Things Applications. *Adv. Electron. Mater.* **5** (no. 11), 1800823 <https://doi.org/10.1002/aelm.201800823> (Nov. 2019).
9. Haras, M. & Skotnicki, T. Thermoelectricity for IoT – A review. *Nano Energy*. **54**, 461–476 <https://doi.org/10.1016/j.nanoen.2018.10.013> (Dec. 2018).
10. Mortimer, R. J., Dyer, A. L. & Reynolds, J. R. Electrochromic organic and polymeric materials for display applications. *Displays*. **27** (no. 1), 2–18 <https://doi.org/10.1016/j.displa.2005.03.003> (Jan. 2006).
11. Terrones, H., López-Urías, F. & Terrones, M. “Novel hetero-layered materials with tunable direct band gaps by sandwiching different metal disulfides and diselenides,” *Sci Rep*, vol. 3, no. 1, p. 1549, Dec 2013, doi: 10.1038/srep01549.
12. Briggs, N. *et al.* A roadmap for electronic grade 2D materials. *2D Mater.* **6** (no. 2), 022001 <https://doi.org/10.1088/2053-1583/aaf836> (Jan. 2019).
13. Oh, J., Kim, Y., Chung, S., Kim, H. & Son, J. G. “Fabrication of a MoS₂/Graphene Nanoribbon Heterojunction Network for Improved Thermoelectric Properties,” *Adv. Mater. Interfaces*, p. 1901333, Oct 2019, doi: 10.1002/admi.201901333 .

15. Falconi, C. Piezoelectric nanotransducers. *Nano Energy*. **59**, 730–744 <https://doi.org/10.1016/j.nanoen.2019.03.027> (May 2019).
16. Díaz-Sánchez, J. *et al.* “Complementary electrochromic devices of PANI and PEDOT using the enzymatic poly(gallic acid),” *Solar Energy Materials and Solar Cells*, vol. 200, p. 109973, Sep 2019, doi: 10.1016/j.solmat.2019.109973.
17. Martínez-Cisneros, E. *et al.* “Electromechanical Modeling of MEMS-Based Piezoelectric Energy Harvesting Devices for Applications in Domestic Washing Machines,” *Energies*, vol. 13, no. 3, p. 617, Feb 2020, doi: 10.3390/en13030617.
18. Caballero-Pérez, R. O., Bravo-Castillero, J., Pérez-Fernández, L. D., Rodríguez-Ramos, R. & Sabina, F. J. “Computation of effective thermo-piezoelectric properties of porous ceramics via asymptotic homogenization and finite element methods for energy-harvesting applications,” *Arch Appl Mech*, vol. 90, no. 6, pp. 1415–1429, Jun 2020, doi: 10.1007/s00419-020-01675-6.
19. Marchetti, L., Berg, Y., Mirmotahari, O. & Azadmehr, M. “Bidirectional front-end for piezoelectric resonator,” in 2016 *IEEE 13th International Conference on Networking, Sensing, and Control (ICNSC)*, Mexico City, Mexico, Apr. 2016, pp. 1–4, doi: 10.1109/ICNSC.2016.7479028.
20. Jaffe, B., Cook, W. R. & Jaffe, H. L. *Piezoelectric ceramics* (Academic Press, London, New York, 1971).
21. Aksel, E. & Jones, J. L. “Advances in Lead-Free Piezoelectric Materials for Sensors and Actuators,” *Sensors*, vol. 10, no. 3, pp. 1935–1954, Mar 2010, doi: 10.3390/s100301935.
22. Soergel, E. Piezoresponse force microscopy (PFM). *J. Phys. D: Appl. Phys.* **44** (no. 46), 464003 <https://doi.org/10.1088/0022-3727/44/46/464003> (Nov. 2011).
23. Jungk, T., Hoffmann, Ä. & Soergel, E. Quantitative analysis of ferroelectric domain imaging with piezoresponse force microscopy. *Appl. Phys. Lett.* **89** (no. 16), 163507 <https://doi.org/10.1063/1.2362984> (Oct. 2006).
24. Sappati, K. & Bhadra, S. Piezoelectric Polymer and Paper Substrates: A Review. *Sensors*. **18** (no. 11), 3605 <https://doi.org/10.3390/s18113605> (Oct. 2018).
25. Ahart, M. *et al.* “Origin of morphotropic phase boundaries in ferroelectrics,” *Nature*, vol. 451, no. 7178, pp. 545–548, Jan. 2008, doi: 10.1038/nature06459.
26. Guan, Z. *et al.* Identifying intrinsic ferroelectricity of thin film with piezoresponse force microscopy. *AIP Advances*. **7** (no. 9), 095116 <https://doi.org/10.1063/1.4999199> (Sep. 2017).
27. Kholkin, A. L., Bdikin, I. K., Kiselev, D. A., Shvartsman, V. V. & Kim, S. H. “Nanoscale characterization of polycrystalline ferroelectric materials for piezoelectric applications,” *J Electroceram*, vol. 19, no. 1, pp. 83–96, Oct 2007, doi: 10.1007/s10832-007-9045-2.
28. Roelofs, A., Schneller, T., Szot, K. & Waser, R. Towards the limit of ferroelectric nanosized grains. *Nanotechnology*. **14** (no. 2), 250–253 <https://doi.org/10.1088/0957-4484/14/2/328> (Feb. 2003).
29. Maldonado-Orozco, M. C. *et al.* Absence of ferromagnetism in ferroelectric Mn-doped BaTiO₃ nanofibers. *J Am Ceram Soc*. **102** (no. 5), 2800–2809 <https://doi.org/10.1111/jace.16179> (May 2019).

30. Zúñiga, V. T., Carmona, S. G. & Morales Saavedra, O. G. Electromechanical characterization of didactical piezoelectric sensors based on crystalline grade PET. *J. Phys.: Conf. Ser.* **1221**, 012059 <https://doi.org/10.1088/1742-6596/1221/1/012059> (Jun. 2019).
31. Zaki, A., Elsimary, H. & Zaghloul, M. "Miniature SAW device using MEMS technology," *Microelectronics Journal*, vol. 38, no. 3, pp. 426–429, Mar 2007, doi: 10.1016/j.mejo.2006.11.010.
32. Rupitsch, S. J. *Piezoelectric Sensors and Actuators: Fundamentals and Applications* (Springer Berlin Heidelberg, Berlin, Heidelberg, 2019).
33. Panda, P. K. Review: environmental friendly lead-free piezoelectric materials. *J Mater Sci.* **44**, 195049–195062 <https://doi.org/10.1007/s10853-009-3643-0> (Oct. 2009).
34. Saito, Y. *et al.* "Lead-free piezoceramics," *Nature*, vol. 432, no. 7013, pp. 84–87, Nov. 2004, doi: 10.1038/nature03028.
35. Damjanovic, D., Klein, N., Li, J., Porokhonsky, V. & "WHAT CAN BE EXPECTED FROM LEAD-FREE PIEZOELECTRIC MATERIALS.," *Funct. Mater. Lett.*, vol. 03, no. 01, pp. 5–13, Mar. 2010, doi: 10.1142/S1793604710000919.
36. Oh, H. & Dayeh, S. A. Physics-Based Device Models and Progress Review for Active Piezoelectric Semiconductor Devices. *Sensors.* **20**, 143872 <https://doi.org/10.3390/s20143872> (Jul. 2020).
37. Gullapalli, H. *et al.* "Flexible Piezoelectric ZnO-Paper Nanocomposite Strain Sensor," *Small*, vol. 6, no. 15, pp. 1641–1646, Jul. 2010, doi: 10.1002/sml.201000254.
38. Banno, H. & Tsunooka, T. "Piezoelectric Properties and Temperature Dependences of Resonant Frequency of WO₃-MnO₂-Modified Ceramics of Pb(Zr-Ti)O₃," *Jpn. J. Appl. Phys.*, vol. 6, no. 8, pp. 954–962, Aug 1967, doi: 10.1143/JJAP.6.954.
39. Zong, X., Yang, Z., Li, H. & Yuan, M. "Effects of WO₃ addition on the structure and electrical properties of Pb₃O₄ modified PZT–PFW–PMN piezoelectric ceramics," *Materials Research Bulletin*, vol. 41, no. 8, pp. 1447–1454, Aug 2006, doi: 10.1016/j.materresbull.2006.02.002.
40. Zhong, N., Dong, X. L., Sun, D., Xiang, P. & Du, H. "Electrical properties of Pb(Mg_{1/3}Nb_{2/3})O₃–PbTiO₃ ceramics modified with WO₃," *Materials Research Bulletin*, vol. 39, no. 2, pp. 175–184, Feb 2004, doi: 10.1016/j.materresbull.2003.10.007.
41. Slimani, Y. *et al.* Role of WO₃ nanoparticles in electrical and dielectric properties of BaTiO₃–SrTiO₃ ceramics. *J Mater Sci: Mater Electron.* **31** (no. 10), 7786–7797 <https://doi.org/10.1007/s10854-020-03317-7> (May 2020).
42. Chen, Y. *et al.* Polarization-Enhanced direct Z-scheme ZnO-WO₃ – x nanorod arrays for efficient piezoelectric-photoelectrochemical Water splitting. *Appl. Catal. B.* **259**, 118079 <https://doi.org/10.1016/j.apcatb.2019.118079> (Dec. 2019).
43. Corby, S., Francàs, L., Kafizas, A. & Durrant, J. R. Determining the role of oxygen vacancies in the photoelectrocatalytic performance of WO₃ for water oxidation. *Chem. Sci.* **11** (no. 11), 2907–2914 <https://doi.org/10.1039/C9SC06325K> (2020).
44. Soltani, T., Tayyebi, A., Hong, H., Mirfasih, M. H. & Lee, B. K. "A novel growth control of nanoplates Loading [MathJax]/jax/output/CommonHTML/jax.js d tungsten vacancies for efficient photoelectrochemical water

- splitting performance,” *Solar Energy Materials and Solar Cells*, vol. 191, pp. 39–49, Mar 2019, doi: 10.1016/j.solmat.2018.10.019.
45. Kim, Y., Alexe, M. & Salje, E. K. H. Nanoscale properties of thin twin walls and surface layers in piezoelectric $\text{WO}_3 - x$. *Appl. Phys. Lett.* **96** (no. 3), 032904 <https://doi.org/10.1063/1.3292587> (Jan. 2010).
 46. Olivas-Ortega, D. E., Ramos-Cano, J., Talamantes-Soto, R. P., Lopez-Melendez, C. & Hurtado-Macias, A. “Nano-Mechanical and Piezoelectric Properties on PZT Thin Films,” *Microsc Microanal*, vol. 24, no. S1, pp. 2236–2237, Aug 2018, doi: 10.1017/S1431927618011662.
 47. Mohanty, D. *et al.* “Synthesis and piezoelectric response of cubic and spherical LiNbO_3 nanocrystals,” *RSC Adv.*, vol. 2, no. 5, p 1913, 2012, doi: 10.1039/c2ra00628f.
 48. Zúñiga, V. T., Carmona, S. G. & Morales Saavedra, O. G. Electromechanical characterization of didactical piezoelectric sensors based on crystalline grade PET. *J. Phys.: Conf. Ser.* **1221**, 012059 <https://doi.org/10.1088/1742-6596/1221/1/012059> (Jun. 2019).
 49. Berak, J. M. & Sienko, M. J. Effect of oxygen-deficiency on electrical transport properties of tungsten trioxide crystals. *Journal of Solid State Chemistry.* **2** (no. 1), 109–133 [https://doi.org/10.1016/0022-4596\(70\)90040-X](https://doi.org/10.1016/0022-4596(70)90040-X) (Jun. 1970).
 50. Deb, S. K. Opportunities and challenges in science and technology of WO_3 for electrochromic and related applications. *Solar Energy Materials and Solar Cells.* **92** (no. 2), 245–258 <https://doi.org/10.1016/j.solmat.2007.01.026> (Feb. 2008).
 51. Greiner, M. T., Chai, L., Helander, M. G., Tang, W. M. & Lu, Z. H. “Transition Metal Oxide Work Functions: The Influence of Cation Oxidation State and Oxygen Vacancies,” *Adv. Funct. Mater.*, vol. 22, no. 21, pp. 4557–4568, Nov 2012, doi: 10.1002/adfm.201200615.
 52. Koo, B. R. & Ahn, H. J. Fast-switching electrochromic properties of mesoporous WO_3 films with oxygen vacancy defects. *Nanoscale.* **9**, 4517788–4517793 <https://doi.org/10.1039/C7NR06796H> (2017).
 53. Lee, C. T. *et al.* “Investigation of Microstructure, Electrical and Optical Properties of WO_3 Film by RF Magnetron Sputtering with Ar/H_2 ,” *AMR*, vol. 123–125, pp. 983–986, Aug 2010, doi: 10.4028/www.scientific.net/AMR.123-125.983.
 54. Lee, S., Yun, K. H. & Kim, D. Electroforming-less and multi-level resistive switching characteristics in tungsten oxide thin film. *Thin Solid Films.* **674**, 91–96 <https://doi.org/10.1016/j.tsf.2019.02.012> (Mar. 2019).
 55. Sachs, M. *et al.* “Effect of oxygen deficiency on the excited state kinetics of WO_3 and implications for photocatalysis,” *Chem Sci*, vol. 10, no. 22, pp. 5667–5677, Jun. 2019, doi: 10.1039/c9sc00693a.
 56. Won, S., Lee, S. Y., Park, J. & Seo, H. Forming-less and Non-Volatile Resistive Switching in WO_x by Oxygen Vacancy Control at Interfaces. *Sci Rep.* **7** (no. 1), 10186 <https://doi.org/10.1038/s41598-017-10851-8> (Dec. 2017).
 57. Manciu, F. S. *et al.* “Spectroscopic analysis of tungsten oxide thin films,” *J. Mater. Res.*, vol. 25, no. 557 <https://doi.org/10.1016/j.jmr.2010.0294>.

58. Hamdi, H., Salje, E. K. H., Ghosez, P. & Bousquet, E. First-principles re-investigation of bulk WO₃. *Phys. Rev. B.* **94**, 24245124 <https://doi.org/10.1103/PhysRevB.94.245124> (Dec. 2016).
59. Ramana, C. V., Utsunomiya, S., Ewing, R. C., Julien, C. M. & Becker, U. "Structural Stability and Phase Transitions in WO₃ Thin Films," *J. Phys. Chem. B*, vol. 110, no. 21, pp. 10430–10435, Jun 2006, doi: 10.1021/jp056664i.
60. Vemuri, R. S., Carbjal-Franco, G., Ferrer, D. A., Engelhard, M. H. & Ramana, C. V. "Physical properties and surface/interface analysis of nanocrystalline WO₃ films grown under variable oxygen gas flow rates," *Applied Surface Science*, vol. 259, pp. 172–177, Oct 2012, doi: 10.1016/j.apsusc.2012.07.014.
61. Enriquez-Carrejo, J. L., Ramos, M. A., Mireles-Jr-Garcia, J. & Hurtado-Macias, A. Nano-mechanical and structural study of WO₃ thin films. *Thin Solid Films.* **606**, 148–154 <https://doi.org/10.1016/j.tsf.2016.03.054> (May 2016).
62. Woodward, P. M., Sleight, A. W. & Vogt, T. "Ferroelectric Tungsten Trioxide," *Journal of Solid State Chemistry*, vol. 131, no. 1, pp. 9–17, Jun 1997, doi: 10.1006/jssc.1997.7268.
63. Locherer, K. R., Swainson, I. P. & Salje, E. K. H. Transition to a new tetragonal phase of WO₃: crystal structure and distortion parameters. *J. Phys.: Condens. Matter.* **11**, 214143–214156 <https://doi.org/10.1088/0953-8984/11/21/303> (May 1999).
64. Li, M. *et al.* Effect of hydrogen on the integrity of aluminium–oxide interface at elevated temperatures. *Nat Commun.* **8** (no. 1), 14564 <https://doi.org/10.1038/ncomms14564> (Apr. 2017).
65. Sequeira, C. A. C., Rodrigues, L. F. F. T. T. G. & Santos, D. M. F. Cation Diffusivity in Nonstoichiometric Tungsten Trioxide Films. *ECS J. Solid State Sci. Technol.* **1** (no. 5), 136–139 <https://doi.org/10.1149/2.010205jss> (2012).
66. Kavitha, V. S. *et al.* "Tb³⁺-doped WO₃ thin films: A potential candidate in white light emitting devices," *Journal of Alloys and Compounds*, vol. 788, pp. 429–445, Jun 2019, doi: 10.1016/j.jallcom.2019.02.222.
67. Bose, R. J., Kavitha, V. S., Sudarsanakumar, C. & Pillai, V. P. M. Phase modification and surface plasmon resonance of Au/WO₃ system. *Appl. Surf. Sci.* **379**, 505–515 <https://doi.org/10.1016/j.apsusc.2016.04.100> (Aug. 2016).
68. Ibrahim, A. B. M. A., Murgan, R., Abd Rahman, M. K. & Osm, J. "Morphotropic Phase Boundary in Ferroelectric Materials," in *Ferroelectrics - Physical Effects*, M. Lallart, Ed. InTech 2011.
69. Boll, T., Unocic, K. A., Pint, B. A. & Stiller, K. "Interfaces in Oxides Formed on NiAlCr Doped with Y, Hf, Ti, and B," *Microsc Microanal*, vol. 23, no. 2, pp. 396–403, Apr 2017, doi: 10.1017/S1431927617000186.
70. Thummavichai, K. *et al.* "Low Temperature Annealing Improves the Electrochromic and Degradation Behavior of Tungsten Oxide (WO_x) Thin Films," *J. Phys. Chem. C*, vol. 121, no. 37, pp. 20498–20506, Sep 2017, doi: 10.1021/acs.jpcc.7b06300.
71. Díaz-Reyes, J., Dorantes-García, V., Pérez-Benítez, A. & Balderas-López, J. A. "Obtaining of films of tungsten trioxide (WO₃) by resistive heating of a tungsten filament," p.6, 2008.

72. Gangwar, J., Gupta, B. K., Tripathi, S. K. & Srivastava, A. K. Phase dependent thermal and spectroscopic responses of Al₂O₃ nanostructures with different morphogenesis. *Nanoscale*. **7** (no. 32), 13313–13344 <https://doi.org/10.1039/C5NR02369F> (2015).
73. Kalantar-zadeh, K. *et al.* "Synthesis of Atomically Thin WO₃ Sheets from Hydrated Tungsten Trioxide," *Chem. Mater.*, vol. 22, no. 19, pp. 5660–5666, Oct 2010, doi: 10.1021/cm1019603.
74. Horsley, J. A., Wachs, E., Brown, J. M., Via, H. & Hardcastle, F. D. "Structure of Surface Tungsten Oxide Species in the WO/Al₂O₃ Supported Oxide System from X-ray Absorption Near-Edge Spectroscopy and Raman Spectroscopy," p.7.
75. Chen, P. W. *et al.* "Fast response of complementary electrochromic device based on WO₃/NiO electrodes," *Sci. Rep.*, vol. 10, no. 1, p. 8430, Dec 2020, doi: 10.1038/s41598-020-65191-x.
76. Li, S., Yao, Z., Zhou, J., Zhang, R. & Shen, H. Fabrication and characterization of WO₃ thin films on silicon surface by thermal evaporation. *Mater. Lett.* **195**, 213–216 <https://doi.org/10.1016/j.matlet.2017.02.078> (May 2017).

Figures

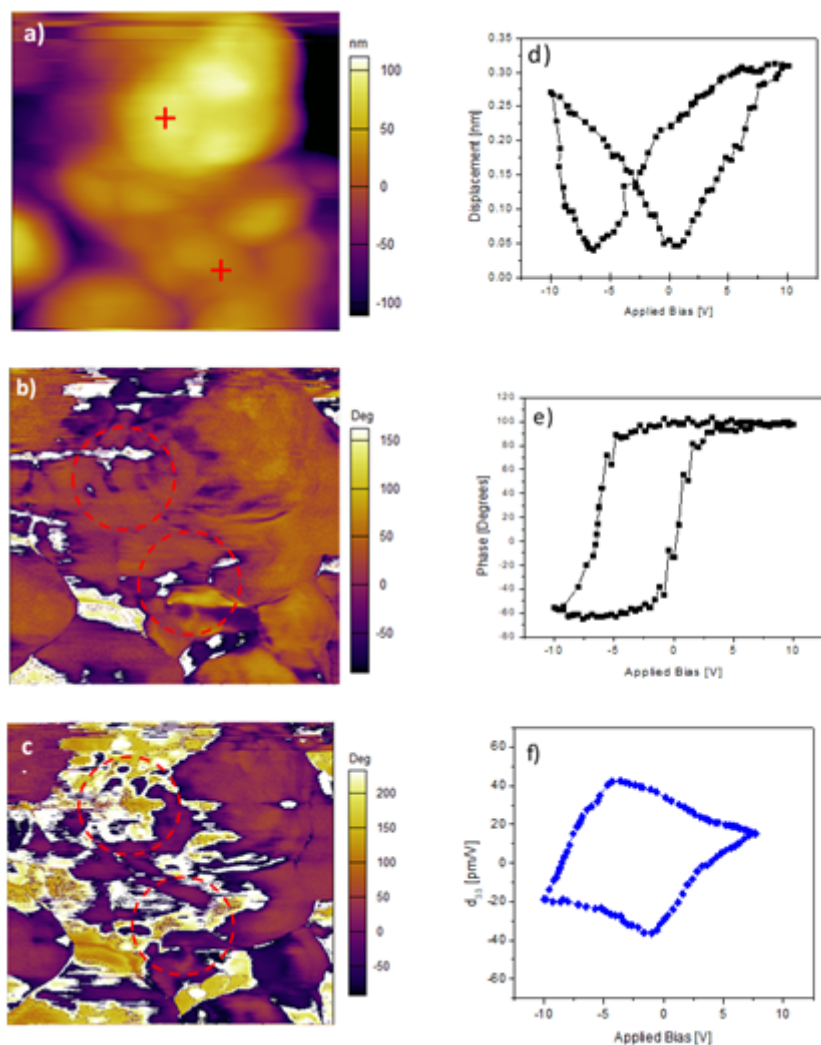


Figure 1

a) Topography in contact mode of the representative sample WO₃ thin film annealing at 400°C, b) and c) is the PFM Signal Phase before and after measurements the local hysteresis loops. d) Amplitude, e) phase, and f) piezo response (d33) versus AC Applied bias voltage of WO₃ thin film annealed at 400°C.

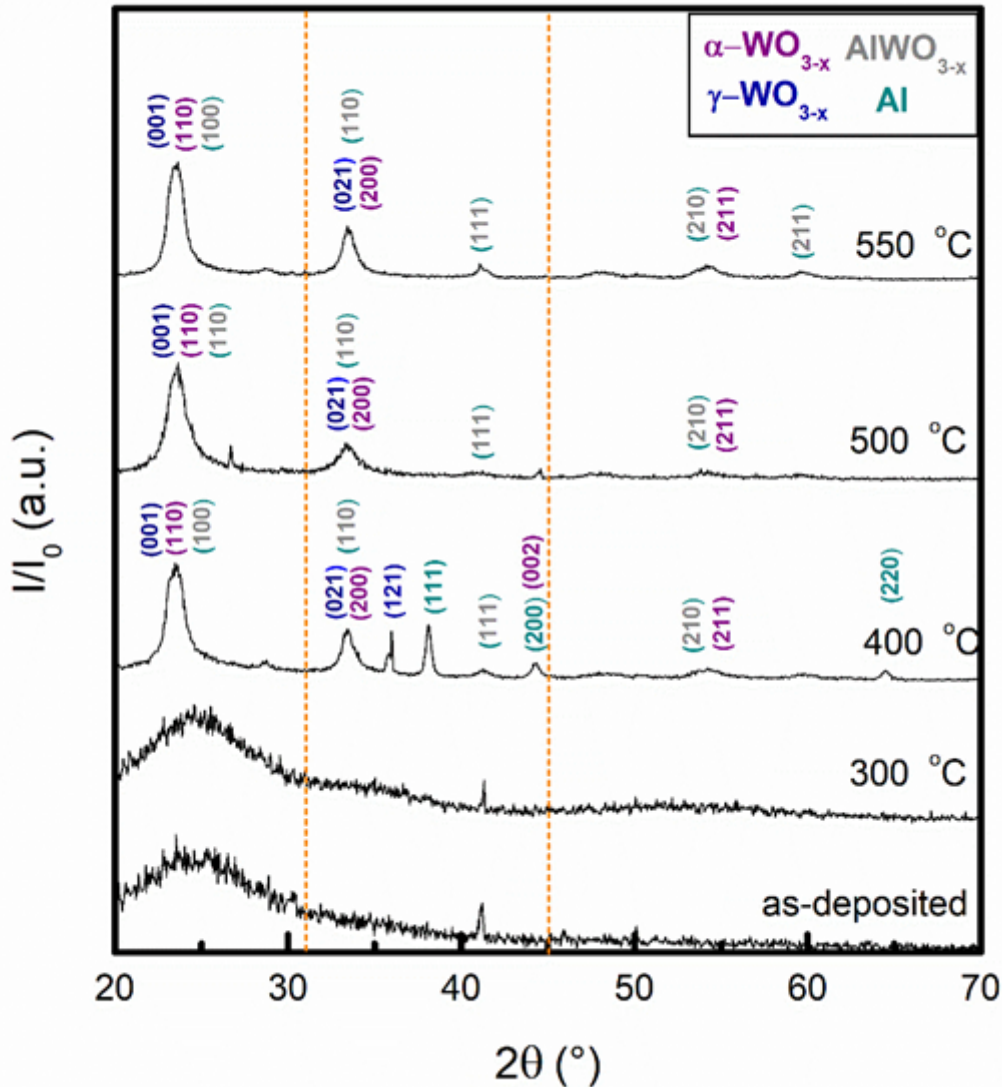


Figure 2

Grazing incidence X-ray diffraction pattern for all as-deposited WO₃ thin films over sapphire. GIXRD measurements were performed in samples annealed at 300 °C, 400 °C, 500 °C, 550 °C, and room-temperature as reference. The sample at 300 °C presents an amorphous structure, while 400 °C shows a mixture of cubic Al, monoclinic and tetragonal WO₃ phases. Sample at 500 °C presents a mixture of monoclinic WO₃ and cubic Al-WO_x. Finally, the sample annealed at 550 °C consists of tetragonal WO₃ and cubic Al-WO_x phase. (It is possible to observe the evolution of crystallographic structures between $2\theta = 32^\circ$ and 46° as indicated by orange dotted box).

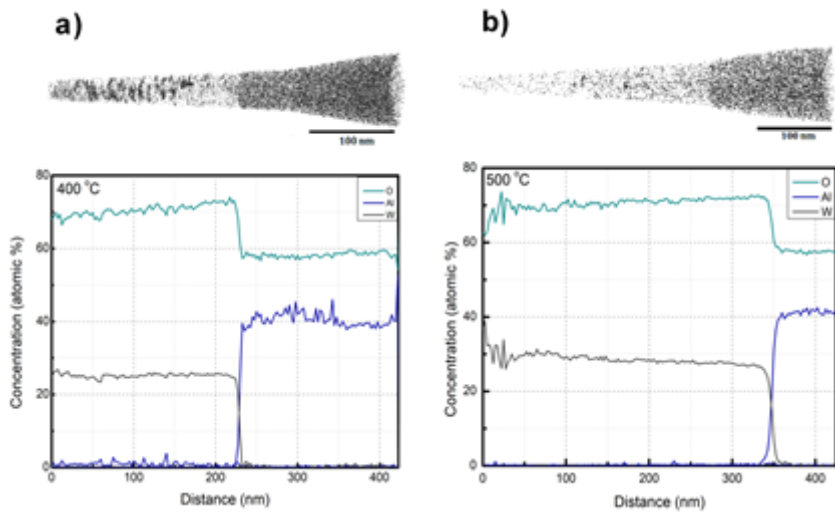


Figure 3

A series of atom probe tomography with corresponding concentration profiles for 400 °C and 500 °C WO_{3-x} thin films as-deposited over Al_2O_3 substrates. a) Sample annealed at 400 °C where it is possible to observe some Al clusters (grey color indicated by the arrow). b) Sample annealed at 500 °C with no traces of aluminum clusters. The composition profiles were created with a bin width of 2.5 nm and background corrected with IVAS 3.6.14 obtained along the long axis of the images corresponding to film growth direction.